Journal of Materials Chemistry C

PAPER

View Article Online
View Journal | View Issue

Check for updates

Cite this: J. Mater. Chem. C, 2019, 7, 3889

Influence of the aqueous solution composition on the morphology of $Zn_{1-x}Mg_xO$ films deposited by spray pyrolysis†

Nina Winkler, *[ab] Rachmat Adhi Wibowo, [a] Wolfgang Kautek [b] and Theodoros Dimopoulos *[a]

Received 3rd December 2018,
Accepted 22nd February 2019

DOI: 10.1039/c8tc06097e

rsc.li/materials-c

Tailoring the band gap of metal oxides is an attractive property for various device applications. Zinc–magnesium-oxide ($Zn_{1-x}Mg_xO$) is a sustainable material that allows control of the energy band gap through the Mg content. To reduce the deposition costs of $Zn_{1-x}Mg_xO$, solution-based techniques can be employed. This study investigates spray-pyrolysis as a versatile, environment-friendly, solution-based deposition method to fabricate $Zn_{1-x}Mg_xO$ films with morphology and properties that strongly depend on the composition of the water-based precursor solution. Films that are either compact or covered with nanorods are obtained, with tunable amounts of incorporated Mg and corresponding band gap values. In order to show the applicability of these films, $Zn_{1-x}Mg_xO$ was sprayed onto transparent conducting oxide substrates that are commonly used in various devices, such as solar cells with superstrate architecture.

Open Access Article. Published on 13 March 2019. Downloaded on 1/14/2026 9:50:56 AM.
This article is licensed under a Creative Commons Attribution 3.0 Unported Licence.

1. Introduction

Oxide-based wide-band gap materials are attractive for an extensive range of applications, such as photovoltaics,[1–3] functional coatings,[4,5] (opto)electronic devices[6–8] or sensors.[9,10] Among them, ZnO is one of the most investigated metal oxides, because of its facile fabrication and doping, especially by low-cost solution-based techniques.[11–13] ZnO can be doped with group-13 elements to enhance the intrinsic n-type conductivity or with divalent elements such as Mg or Cd, which increase or decrease the band gap due to differences in the electron affinity.[14,15] The tunability of the band gap with Mg incorporation renders $Zn_{1-x}Mg_xO$ especially interesting for semiconductor devices, as the energy band alignment at the heterojunction is of utmost importance. An example is given by Hariskos *et al.* who reported the application of $Zn_{1-x}Mg_xO$ as n-type buffer layer in $Cu(In,Ga)(Se,S)_2$-based thin film solar cells[16] or Minami *et al.* who applied a $Zn_{1-x}Mg_xO$ buffer layer in Cu_2O-type solar cells.[17]

Although $Zn_{1-x}Mg_xO$ can be deposited by a variety of vacuum-based deposition techniques, such as pulsed laser deposition (PLD),[18] sputtering,[19] molecular beam epitaxy (MBE)[20] or atomic layer deposition (ALD),[21] solution-based methods are particularly interesting regarding deposition costs. Solution-based $Zn_{1-x}Mg_xO$ deposition includes chemical bath deposition (CBD),[22] electrochemical deposition (ECD),[23] and sol–gel techniques.[24] The first two take place close to ambient temperature, but they have the disadvantage that the thermodynamic solubility limit of MgO in ZnO is ~4%.[25] Sol–gel techniques can achieve higher Mg incorporation up to 23%,[24] but require a high temperature (>500 °C) annealing step for sufficient film quality.

Spray pyrolysis is a versatile solution-based growth technique, which yields high-quality ZnO films at temperatures below 400 °C.[26–28] Further, this method is easy to upscale and, therefore, suitable for large area deposition. In spray pyrolysis a precursor solution, containing volatile metal salts, forms a mist of droplets that are directed onto a heated substrate. For the droplet generation many techniques are available. Among them, the ultrasonic atomizing system has been proven to be precise, controllable and repeatable.[29]

$Zn_{1-x}Mg_xO$ films deposited by spray pyrolysis have been reported frequently,[15,30–41] but in the majority of the reports toxic or flammable solvents, such as methanol[30–32] or ethanol,[15,34,35] are used. Studies on water-based solutions are rare.[36,37,40,41] Moreover, due to the unfavorable properties of water as a solvent in spray pyrolysis (such as strong hydrogen bonds and a high boiling point),[27] temperatures above >400 °C are commonly employed.[36,37] Among the studies using water-based solutions and temperatures below 400 °C, none achieved Mg incorporation larger than 10 mol%.[40,41]

For certain device applications, the use of nanostructures instead of compact films can be an advantage.[42–44] For the same

[a] AIT Austrian Institute of Technology, Center for Energy, Photovoltaic Systems, Giefinggasse 6, A-1210 Vienna, Austria. E-mail: nina.winkler@ait.ac.at, theodoros.dimopoulos@ait.ac.at
[b] University of Vienna, Department of Physical Chemistry, Währinger Straße 42, A-1090 Vienna, Austria

† Electronic supplementary information (ESI) available. See DOI: 10.1039/c8tc06097e

Open Access Article. Published on 13 March 2019. Downloaded on 1/14/2026 9:50:56 AM.
This article is licensed under a Creative Commons Attribution 3.0 Unported Licence.

reasons as for compact films, it is highly desired to deposit nanostructures with a tailored band gap. A common approach to obtain Mg-doped ZnO nanorods from aqueous solutions is hydrothermal deposition, but so far the amount of incorporated Mg by this technique was limited to below 1%.[45,46] Up to now, there is no report on $Zn_{1-x}Mg_xO$ nanorod deposition by a one-step spray pyrolysis process.

In this work $Zn_{1-x}Mg_xO$ was deposited by ultrasonic spray pyrolysis (USP) from water-based solutions at 360 °C, in air. Solely low-cost and environment-friendly raw materials were chosen for the precursor solution. This study elucidates the effect of the solution composition on the deposited $Zn_{1-x}Mg_xO$ films and presents a novel, one-step synthesis approach to obtain $Zn_{1-x}Mg_xO$ films that are either compact or covered with nanorods on various substrates. The Mg incorporation in the $Zn_{1-x}Mg_xO$ films was investigated and optical band gaps were determined. In order to show the applicability of these films in applications, $Zn_{1-x}Mg_xO$ was sprayed onto three different transparent conducting oxide substrates which are commonly used as electrodes in devices.

2. Experimental

2.1. Spray pyrolysis set-up

USP was carried out in a Sono-Tek Exacta Coat® system, using a Sono-Tek Impact® 120 kHz nozzle in the horizontal geometry with an applied power of 3.5 W. The solution flow rate was kept at 0.8 ml min^{-1} and compressed air (0.5 bar) was used as the carrier gas. The substrate-to-nozzle distance was kept at 200 mm and the scanning speed of the nozzle over the substrate was 25 mm s^{-1}. The number of spraying cycles over the substrate was for all experiments fixed to 80 repetitions, unless otherwise stated, resulting in a film thickness between 200 and 300 nm. The substrates were heated to 360 °C using a hot plate covered with an aluminium substrate holder.

2.2. Sample preparation and precursor solutions

Borosilicate glass substrates (Schott Nexterion® D, 7.5 × 2.5 cm^2) were ultrasonically cleaned at 50 °C for 30 minutes in Hellmanex® III washing solution, rinsed with deionized water (DI, 18 MΩ cm^{-1}), then rinsed with isopropanol and finally dried in an air stream. Commercial fluorine-doped tin oxide (FTO, 2.2 mm thick, 7 Ω Sq^{-1}, Sigma-Aldrich 735140-5EA) and indium tin oxide glass substrates (ITO, 1 mm thick, Sigma-Aldrich 703192, 8–12 Ω Sq^{-1}) were rinsed with deionized water, rinsed with isopropanol and dried in an air stream. For the preparation of 1.8 μm-thick indium-doped ZnO (IZO) films on borosilicate glass substrates the same recipe as previously reported by our group[47] was used.

In the first set of experiments $Zn_{1-x}Mg_xO$ films were deposited on clean glass substrates using precursor solutions with various concentrations of magnesium dopant and a constant concentration of zinc salt. Metal acetates were chosen as precursor salts due to their low-cost, non-toxicity and suitable properties for spray deposition. The sprayed aqueous solutions A–F contained 0.2 M of zinc acetate dihydrate ($Zn(CH_3COO)_2 \times 2H_2O$, Sigma-Aldrich 96459) and 0, 5, 10, 15, 20 and 30 mol% magnesium acetate tetrahydrate ($Mg(CH_3COO)_2 \times 4H_2O$, Sigma-Aldrich M5661) dissolved in deionized water, as summarized in Table 1. Additionally, the solutions contained 1.4 M acetic acid (CH_3COOH, Sigma-Aldrich A6283) to achieve a lower surface tension, resulting in a smaller droplet size, as well as a pH value suitable for the deposition.

Table 1 Composition of the sprayed solutions

Solution	Concentration $ZnAc_2$ (M)	Mg dopant (mol%)	Acetic acid (M)	pH value
A	0.2	0	1.4	3.60
B	0.2	5	1.4	3.67
C	0.2	10	1.4	3.69
D	0.2	15	1.4	3.74
E	0.2	20	1.4	3.78
F	0.2	30	1.4	3.80
G	0.1	15	1.4	3.60
H	0.4	15	1.4	3.95
I	0.8	15	1.4	4.10
J	0.2	15	0.35	4.44
K	0.2	15	2.8	3.45
L	0.2	15	5.25	3.10

To investigate the influence of the zinc acetate molarity and the solution pH value, solutions G–L were prepared with a constant Mg concentration (15 mol% Mg) and varied zinc acetate molarities or acetic acid concentrations as displayed in Table 1.

For the deposition of nanorods and compact films on different TCO substrates, solutions D and I with 15 mol% Mg and different zinc acetate molarities were sprayed onto IZO, FTO and ITO.

2.3. Film characterization

The film morphology and film thickness were analysed by scanning electron microscopy (SEM, Zeiss Ultra 40), using an in-lens detector and a 5 kV acceleration voltage. The transparency of the films was obtained by Fourier transform infrared spectroscopy (FTIR, Bruker Vertex 70) in the UV/vis/IR range between 300 and 1000 nm. X-ray diffraction (XRD, ThermoFisher Scientific ARL Equinox 100) with Cu-K_α (λ = 1.5419 Å) radiation was used to determine the crystal structure of the deposited films. The elemental composition was determined by inductive coupled plasma spectroscopy (ICP-OES, PerkinElmer Optima 5300 DV). For the ICP-OES measurements liquid samples were prepared by dissolving the $Zn_{1-x}Mg_xO$ films in 1 M ultrapure HNO_3 in an ultrasonic bath for 20 minutes at room temperature. The sheet resistance was measured using a 4-point probe set-up connected to a semiconductor parameter analyzer (Süss MicroTec probes, Agilent 4156 C parameter analyzer). EDX analysis was done on a scanning electron microscope (Zeiss Supra 55 VP) with an accelerating voltage of 3 kV.

3. Results and discussion

3.1. Influence of the solution composition on the deposited $Zn_{1-x}Mg_xO$ structure

3.1.1. Effect of Mg concentration. The addition of Mg acetate to the solution causes a change in the surface morphology from a compact film to nanorods, as seen in the SEM images in

 This journal is © The Royal Society of Chemistry 2019

Open Access Article. Published on 13 March 2019. Downloaded on 1/14/2026 9:50:56 AM.
This article is licensed under a Creative Commons Attribution 3.0 Unported Licence.

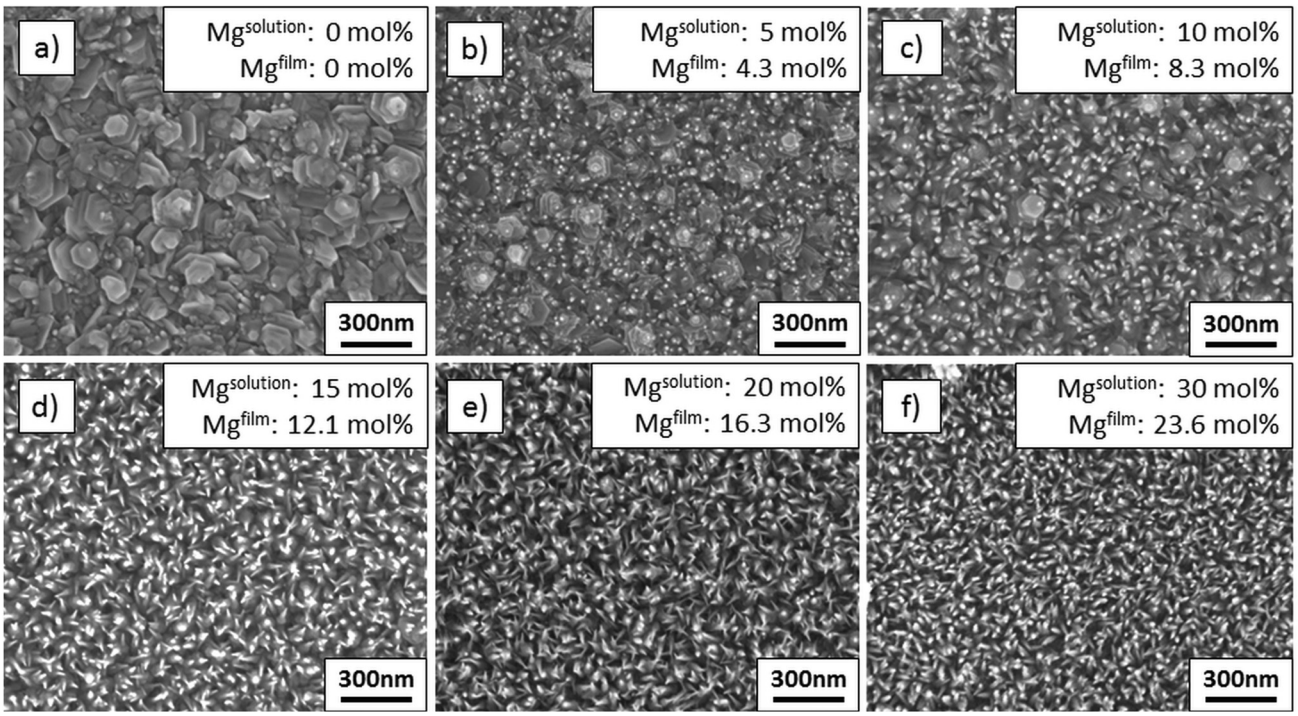

Fig. 1 SEM plane views of films deposited from solutions with varied amounts of Mg: (a) undoped ZnO, (b) 5 mol% Mg, (c) 10 mol% Mg, (d) 15 mol% Mg, (e) 20 mol% Mg, and (f) 30 mol% Mg.

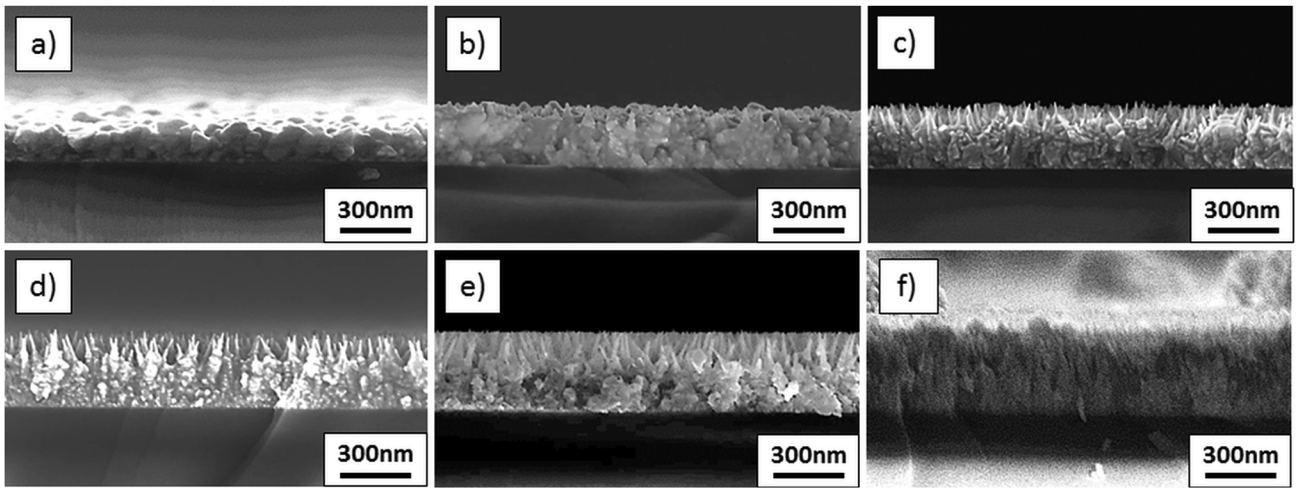

Fig. 2 SEM cross sections of films deposited from solutions with varied amounts of Mg: (a) undoped ZnO, (b) 5 mol% Mg, (c) 10 mol% Mg, (d) 15 mol% Mg, (e) 20 mol% Mg, and (f) 30 mol% Mg.

Fig. 1(a)–(f). Films deposited from the undoped ZnO solution show high surface roughness and pronounced grain facets. With higher Mg content in the solution, an increasing amount of evenly distributed nanorods was observed. SEM cross sections (Fig. 2(a)–(f)) reveal that the films are composed of a first dense $Zn_{1-x}Mg_xO$ part, followed by a part with nanorods. The amount of Mg present in the deposited materials was determined by ICP OES elemental analysis and is listed in Table 2 and shown in Fig. 1.

Independent of the Mg concentration in the solution, X-ray diffractograms demonstrate that all $Zn_{1-x}Mg_xO$ films exhibit a

Table 2 (0001) ZnO 2θ position and Mg content for films obtained from solutions A–E

Solution	Mg in solution (mol%)	$ZnAc_2$ molarity (M)	(0001) ZnO 2θ position	Mg in film from ICP OES (mol%)
A	0	0.2	34.304	0
B	5	0.2	34.333	4.29
C	10	0.2	34.363	8.33
D	15	0.2	34.392	12.08
E	20	0.2	34.421	16.27

Open Access Article. Published on 13 March 2019. Downloaded on 1/14/2026 9:50:56 AM.
This article is licensed under a Creative Commons Attribution 3.0 Unported Licence.

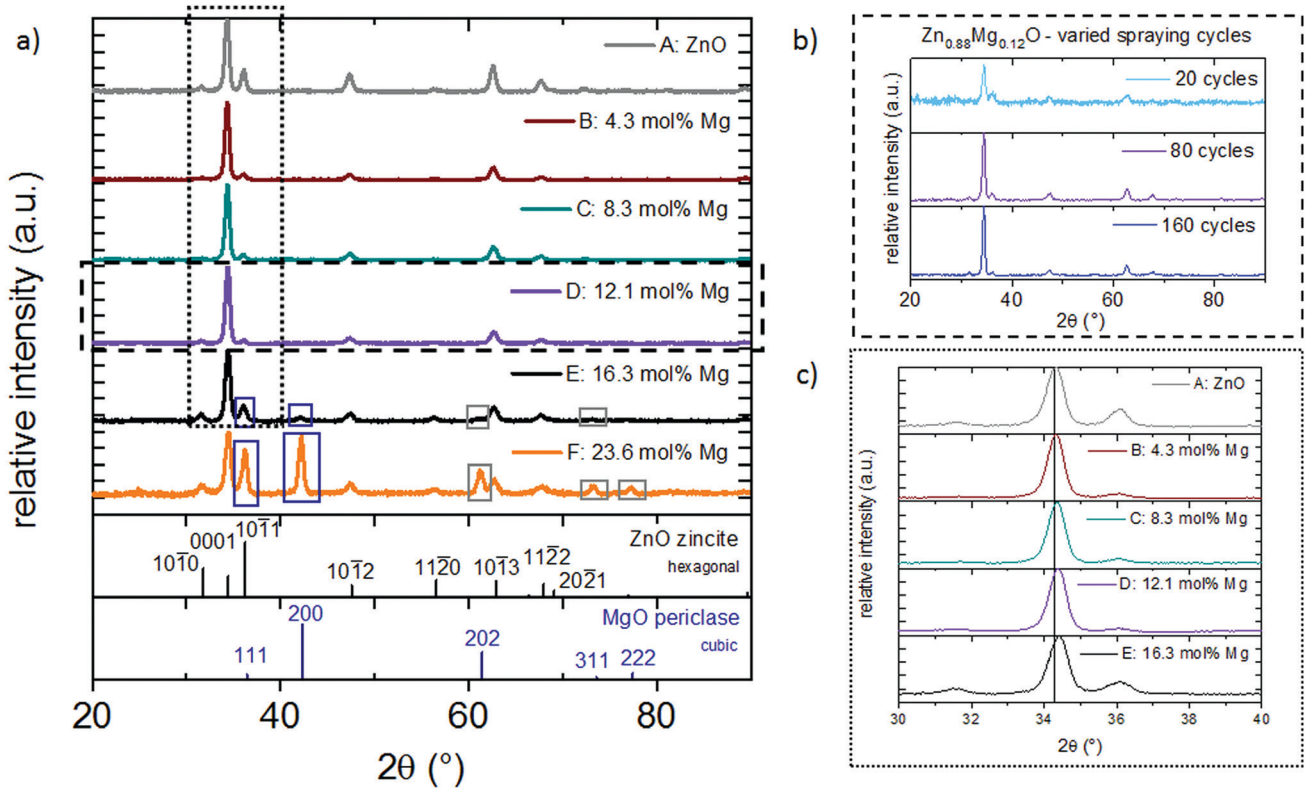

Fig. 3 X-ray diffractograms of films deposited from (a) solutions A–F with varied amounts of Mg, and (b) solution D with a varied number of spraying cycles. (c) (0001) ZnO peak for films deposited from solutions A–E.

preferred {0001} ZnO orientation (Fig. 3(a)). Samples deposited from solutions A–D (up to 15 mol% Mg in the solution) exhibit only the zincite phase (COD database, 96-900-4182), while solutions E (20 mol% Mg in the solution) and F (30 mol% Mg in the solution) result in segregation of a MgO periclase phase (COD database, 96-900-6463) with a preferred {111} and {200} orientation. Grain agglomerates covering the nanorod layer were observed for samples deposited from these solutions as shown in Fig. 4. The agglomerates most likely consist of a mixture of MgO and $Zn_{1-x}Mg_xO$.

Our results suggest a solubility limit of ~20 mol% Mg in the solution (resulting in ~16 mol% Mg in the film) for the experimental conditions of this study. Samples deposited from 30 mol% Mg solutions showed an especially high amount of Mg (23.6 mol%) in the ICP OES, which is attributed to MgO coprecipitation. A variation in spraying cycles for solution D retains the preferred {0001} ZnO crystal orientation (Fig. 3(b)) even for the thinnest film, suggesting that there is no competitive growth in the beginning of the film formation.

One important aspect of this work was the incorporation of Mg into the ZnO lattice. To verify that Mg is indeed substituting Zn atoms in the lattice and not solely occupying interstitial sites, XRD peaks were studied. Since the ionic radius of the tetrahedral Mg is slightly smaller (0.57 Å)[48] compared to Zn (0.60 Å),[48] a substitution by this ion results in a minor peak shift to higher 2θ angles. Fig. 3(c) and Table 2 show the {0001} reflection of zincite $Zn_{1-x}Mg_xO$ films deposited from solutions with varied Mg acetate concentrations. In comparison to undoped ZnO, films containing 16 mol% Mg cause a shift of the {0001} reflection from 34.304° to 34.421°. This indicates incorporation of the Mg atom in the ZnO lattice. Peak shifts to higher 2θ angles are commonly observed in $Zn_{1-x}Mg_xO$ prepared by spray pyrolysis and for a similar Mg incorporation range the values obtained in the present study fit well to literature data.[15,40]

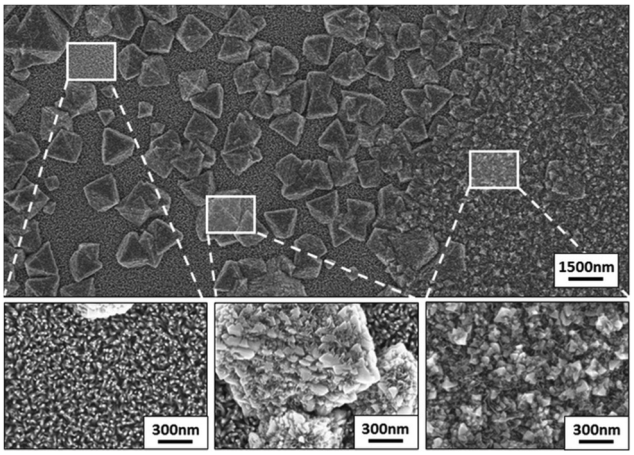

Fig. 4 SEM image (top) of a film deposited from 30 mol% Mg solution F, composed of areas with different morphological features, ranging from nanorods to larger-scale agglomerates, shown in the marked zoomed-in areas (bottom).

 This journal is © The Royal Society of Chemistry 2019

Open Access Article. Published on 13 March 2019. Downloaded on 1/14/2026 9:50:56 AM.
This article is licensed under a Creative Commons Attribution 3.0 Unported Licence.

The formation of nanorods by spray pyrolysis is not a common phenomenon. Nanorod growth is either observed if a seed layer is deposited prior to the spray deposition[49] or at higher temperatures around 500–600 °C.[50,51] The growth evolution of nanorods by addition of Mg can be explained by considering the aspects that influence the film growth in spray pyrolysis. According to Arca *et al.*,[27] the main factors are: (i) the thermal properties of the solvent, (ii) the volatility/decomposition properties of the precursors and (iii) the substrate temperature.

The solvent evaporation is mainly defined by the water : acetic acid ratio, which was fixed for this experimental series. Therefore, this influence can be neglected.

As far as the thermal decomposition of the metal salt precursors is concerned, it is often studied by thermal analysis methods, such as thermogravimetric (TGA) or differential thermal analysis (DTA). These methods usually apply much lower heating rates compared to those that the precursors undergo in the spray pyrolysis process. Although the heating rate has a significant influence on the thermal decomposition, some conclusions could be drawn. Reports on TGA/DTA analysis of $ZnAc_2$ and $MgAc_2$ show that $ZnAc_2$ decomposes completely at a much lower temperature (~300 °C)[52] compared to $MgAc_2$ (~400 °C),[53] at an applied heating rate of 20 °C min^{-1}. Further, for the $ZnAc_2$ decomposition it was proposed that a volatile intermediate tetrahedral cluster of $ZnO_4(CH_3COO)_6$ (I) (basic zinc acetate complex BZA) is formed, which can adsorb on the substrate surface and stepwise decompose to ZnO.[54,55] Such a complex was never reported for $MgAc_2$ decomposition and since Mg^{2+} prefers the octahedral over the tetrahedral complex coordination,[56,57] it may not be favorable. However, there is the possibility that some zinc atoms in the BZA are substituted by magnesium atoms. It is not clear to what extent the decomposition of $ZnAc_2$ is influenced by $MgAc_2$ addition.

The main influence on the growth behaviour most likely arises from the substrate temperature. A possible explanation for the nanorod formation is the modified temperature at the substrate/air interface due to the $Zn_{1-x}Mg_xO$ deposition. Mg doping lowers the thermal conductivity of ZnO,[58,59] resulting in a temperature gradient that favors nanorod growth (see also the schematic growth behaviour in Fig. 5(a)–(c)). At the same time,

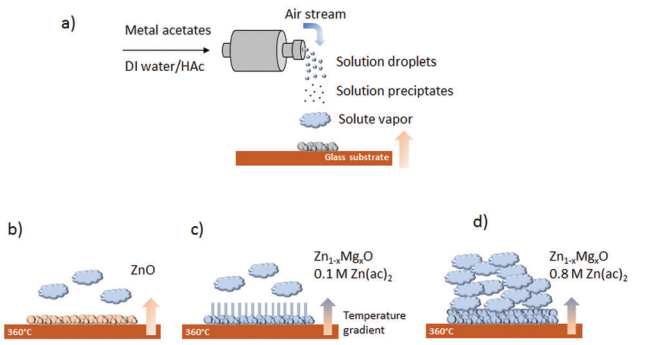

Fig. 5 Schematic of (a) the general spray pyrolysis process, (b) ZnO deposition, (c) $Zn_{1-x}Mg_xO$ nanorod deposition from 0.1 M $Zn(ac)_2$ solution, and (d) $Zn_{1-x}Mg_xO$ film deposition from 0.8 M $Zn(ac)_2$.

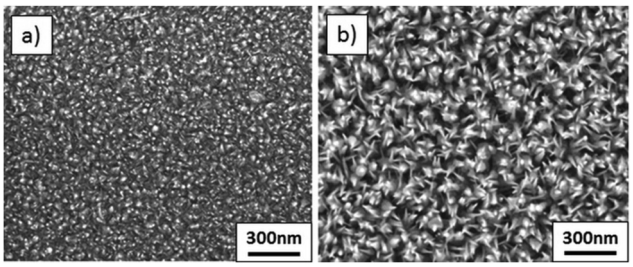

Fig. 6 SEM plane views of films deposited from a 15 mol% Mg solution with a varied number of spraying cycles: (a) 20 cycles, and (b) 160 cycles.

the underlying compact film acts as a seed layer for the growth of nanorods.

To further investigate this behaviour, films were deposited with an increasing number of spraying cycles, namely 20, 80 and 160 cycles, from solution D (15 mol% Mg). Fig. 1(d) and 6(a) and (b) show plain view SEM images of these films and Fig. 2(d) and 7(a) and (b) cross sections. From examination of these images it is concluded that a low number of spraying cycles (fast deposition process, less substrate cooling) results in thin and compact films, while for an increasing number of spraying cycles the nanorod length remains constant, while the thickness of the compact part of the film underneath the nanorods increases. This means that nanorods evolve into a compact film as the spraying proceeds.

To verify that the nanorods indeed consist of $Zn_{1-x}Mg_xO$, EDX analysis of the compact part of the film and the part with the nanorods was realized. For this, separate scans were acquired on the tilted cross section of a film deposited from solution D (with 15 mol% Mg) (see also Fig. S1, ESI†). In both scans, corresponding to the compact and nanorod part of the film, EDX showed signals from Zn and Mg (Fig. S2, ESI†).

3.1.2. Effect of zinc acetate molarity. The zinc acetate ($ZnAc_2$) molarity was adjusted, while maintaining 15 mol% Mg acetate in the solution. A solution containing 15 mol% Mg and 0.2 M zinc acetate resulted previously in the formation of nanorods (see also Fig. 1(d) and 2(d)). It was observed that with increasing $ZnAc_2$ molarity denser films can be obtained, while a lower overall metal salt concentration results in thinner compact films with enlarged nanorods as displayed in Fig. 8(a)–(c) and 9(a)–(c). Independent from the $Zn_{1-x}Mg_xO$ structure, the amount of Mg determined by ICP OES remained unchanged as listed in Table 3 and Fig. 8(a)–(c). This is another indication that the nanorods and the compact film have similar compositions.

Fig. 5(d) shows schematically that a high $ZnAc_2$ molarity results in a large amount of incoming volatile zinc and magnesium species, which hinder the formation of $Zn_{1-x}Mg_xO$ nanorods and

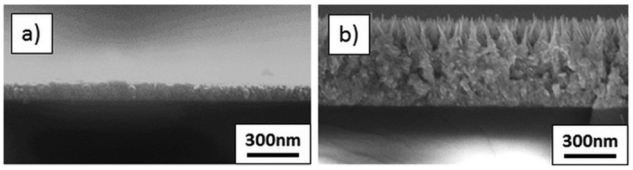

Fig. 7 SEM cross sections of films deposited from a 15 mol% Mg solution with a varied number of spraying cycles: (a) 20 cycles, and (b) 160 cycles.

Open Access Article. Published on 13 March 2019. Downloaded on 1/14/2026 9:50:56 AM.
This article is licensed under a Creative Commons Attribution 3.0 Unported Licence.

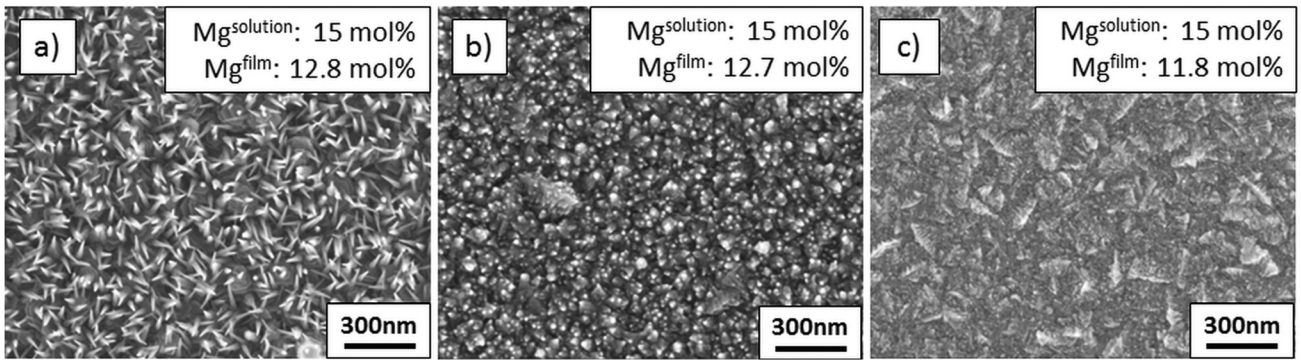

Fig. 8 SEM images of films deposited from solutions with varied zinc acetate molarity (a) G: 0.1 M, (b) H: 0.4 M, and (c) I: 0.8 M.

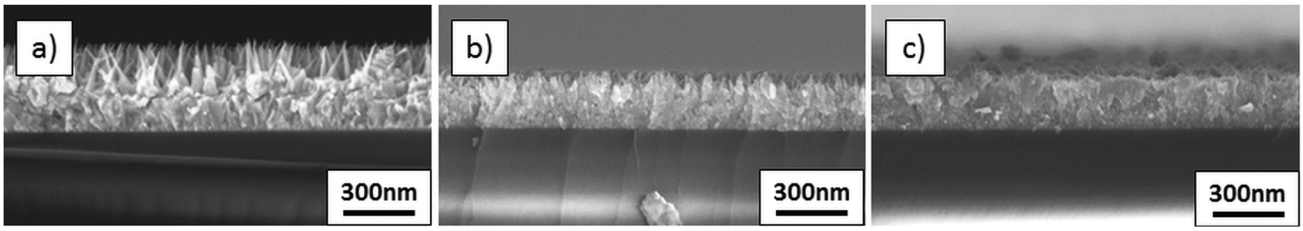

Fig. 9 SEM cross sections of films deposited from solutions with varied zinc acetate molarity (a) G: 0.1 M, (b) H: 0.4 M, and (c) I: 0.8 M.

pack closely forming a compact film. Besides that, as the deposition process is accelerated, there is less surface cooling. At the same time, a higher $ZnAc_2$ molarity increases the pH value from 3.6 to 4.1, resulting in an altered solution speciation of volatile Zn and Mg complexes, which might also affect the film growth.

Upon comparison of the compact ZnO film in Fig. 2(a) with the compact $Zn_{1-x}Mg_xO$ film in Fig. 9(c), one can observe that they possess different surface morphologies (see also plain view SEM images in Fig. 1(a) and 8(c)). Additionally, the XRD diffractograms shown in Fig. 3(a) and 10(a) reveal that they exhibit differing textures.

$Zn_{1-x}Mg_xO$ films stemming from solutions with different $ZnAc_2$ molar concentrations (0.1–0.8 M) have distinctive structural properties. Films deposited from solutions G (0.1 M) and H (0.4 M) show a preferred {0001} ZnO orientation (Fig. 10(a)). Deposition from solution I (0.8 M) gives rise to a polycrystalline ZnO film with higher intensities of the $\{10\bar{1}0\}$ and $\{10\bar{1}1\}$ reflections. The position of the {0001} ZnO peak, as shown in Fig. 10(b) and Table 3, is not altered by a variation in the $ZnAc_2$ molarity. This confirms, together with ICP OES, that Mg incorporation is only dependent on the Mg content in the solution.

In summary, adjustment of the $ZnAc_2$ molarity offers a simple tool to control the film morphology and deposit films with or without nanorods, with various amounts of incorporated Mg.

Table 3 (0001) ZnO 2θ position and Mg content for films obtained from solutions G–I

Solution	Mg in solution (mol%)	$ZnAc_2$ molarity (M)	(0001) ZnO 2θ position	Mg in film from ICP OES (mol%)
G	15	0.1	34.392	12.84
H	15	0.4	34.392	12.72
I	15	0.8	34.392	11.78

3.1.3. Effect of acetic acid concentration. The amount of acetic acid (HAc) was varied to investigate the influence of the solution pH value and of the solvent evaporation behaviour on the $Zn_{1-x}Mg_xO$ morphology. The resulting film morphologies are displayed in Fig. 11(a)–(c). With increasing pH value (lower acetic acid concentration) fewer nanorods are observed. The H_2O : HAc ratio not only has an influence on the temperature during the deposition, it also alters slightly the mean droplet size due to a change in the surface tension.[60] Further, the amounts of volatile Zn and Mg species in the solution depend on the pH value and can also influence the film growth. Compared to the influence of the Mg concentration or the zinc acetate molarity on the $Zn_{1-x}Mg_xO$ morphology, the influence of the acetic acid concentration is less pronounced.

XRD confirmed, as shown in Fig. 12(a), that all films are polycrystalline, with a preferred {0001} ZnO orientation. Films deposited from a solution containing a high acetic acid concentration have a reduced thickness due to the lower heat required for solvent vaporization and the consequential higher effective deposition temperature. Further, a minor {0001} peak shift to higher 2θ angles (see also Fig. 12(b)) can be observed.

3.2. Optical and electrical $Zn_{1-x}Mg_xO$ properties

FTIR spectra (in the UV/vis/IR wavelength region) of the films obtained from all solution compositions are displayed in Fig. 13(a)–(c). For varying Mg concentration (Fig. 13(a)) higher transparencies are observed till 12.1 mol% Mg incorporation, compared to undoped ZnO. Films deposited from solutions E and F with high Mg concentrations exhibit a lower transparency, due to the presence of white MgO precipitates on the film surface. For variations in the $ZnAc_2$ molarity (Fig. 13(b)) and

 This journal is © The Royal Society of Chemistry 2019

Open Access Article. Published on 13 March 2019. Downloaded on 1/14/2026 9:50:56 AM.
This article is licensed under a Creative Commons Attribution 3.0 Unported Licence.

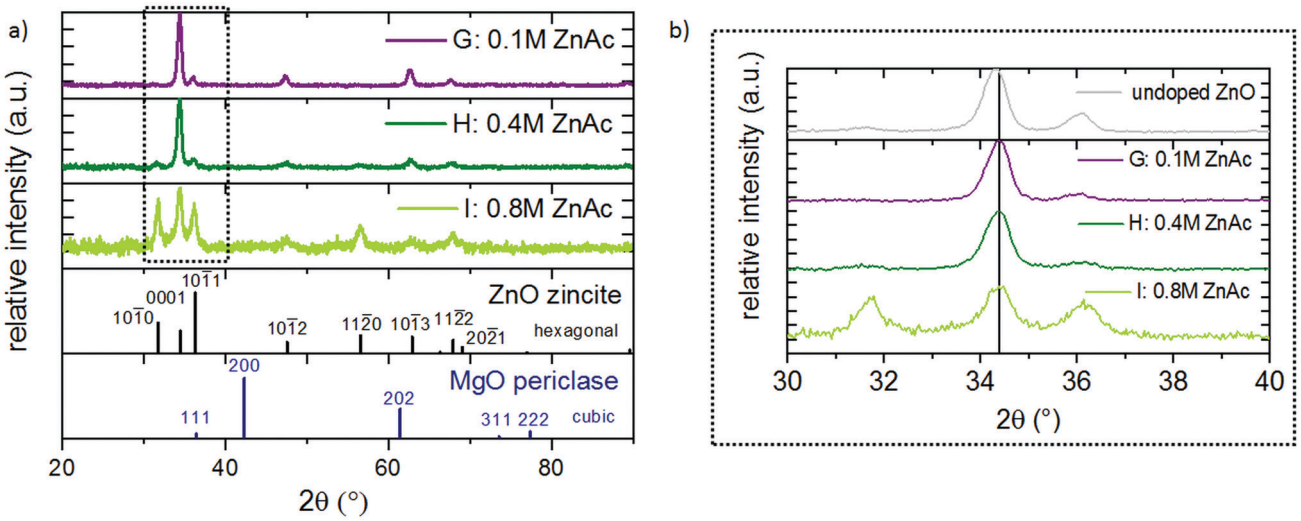

Fig. 10 (a) XRD spectra of films deposited from solutions with 15 mol% Mg with varied zinc acetate molarity, and (b) zoomed in (0001) ZnO peak.

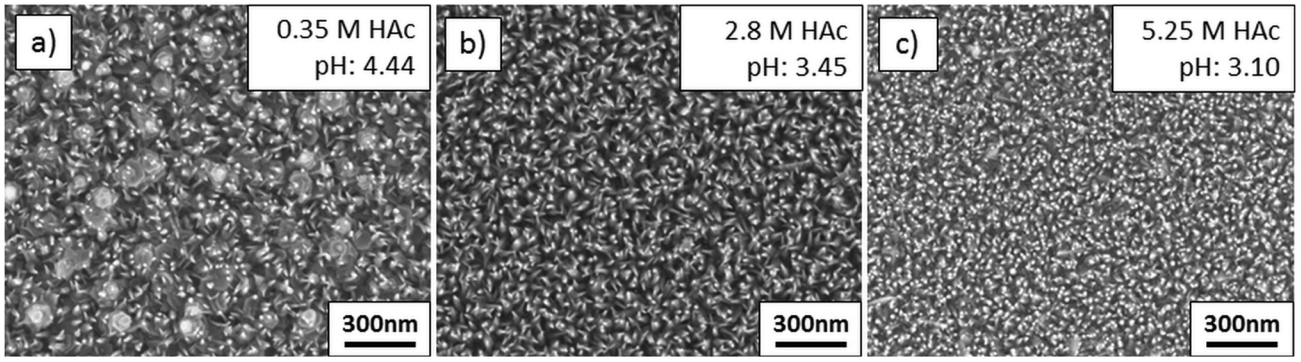

Fig. 11 Films sprayed from solution with various amounts of acetic acid: (a) J: 0.35 M HAc, (b) K: 2.80 HAc, and (c) L: 5.25 M HAc.

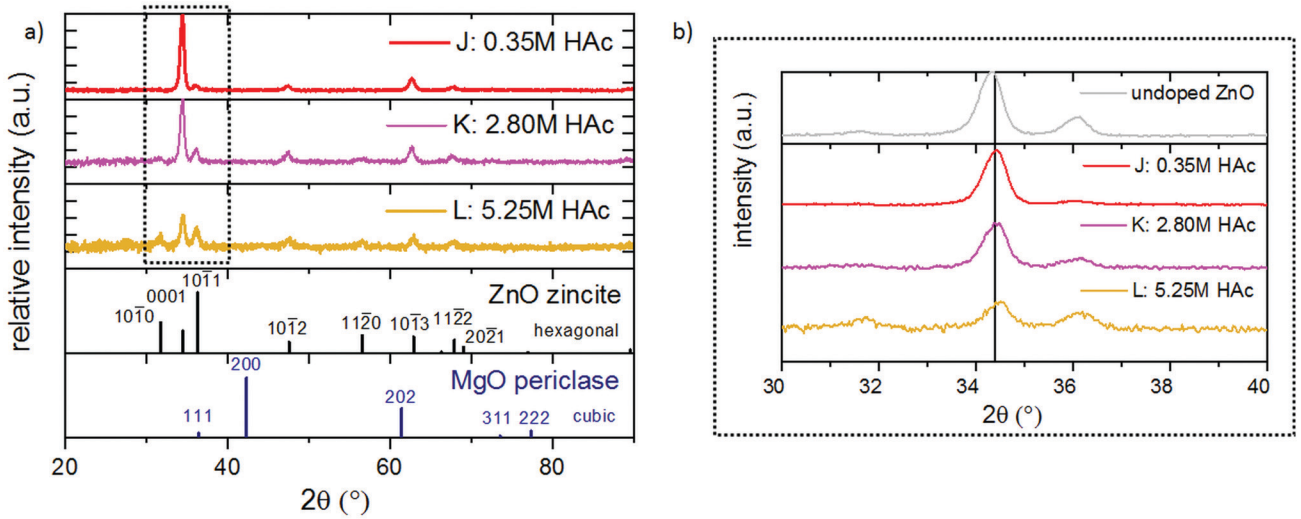

Fig. 12 (a) XRD spectra of films deposited from solutions with 15 mol% Mg and varied acetic acid concentrations, and (b) zoom-in of the (0001) ZnO peak.

the HAc concentration (Fig. 13(c)) the resulting transparency is constant, with values $>80\%$.

Optical band gaps were linearly extrapolated as shown in Fig. 13(d)–(f) from transmittance data using Tauc's relation for

Open Access Article. Published on 13 March 2019. Downloaded on 1/14/2026 9:50:56 AM.
This article is licensed under a Creative Commons Attribution 3.0 Unported Licence.

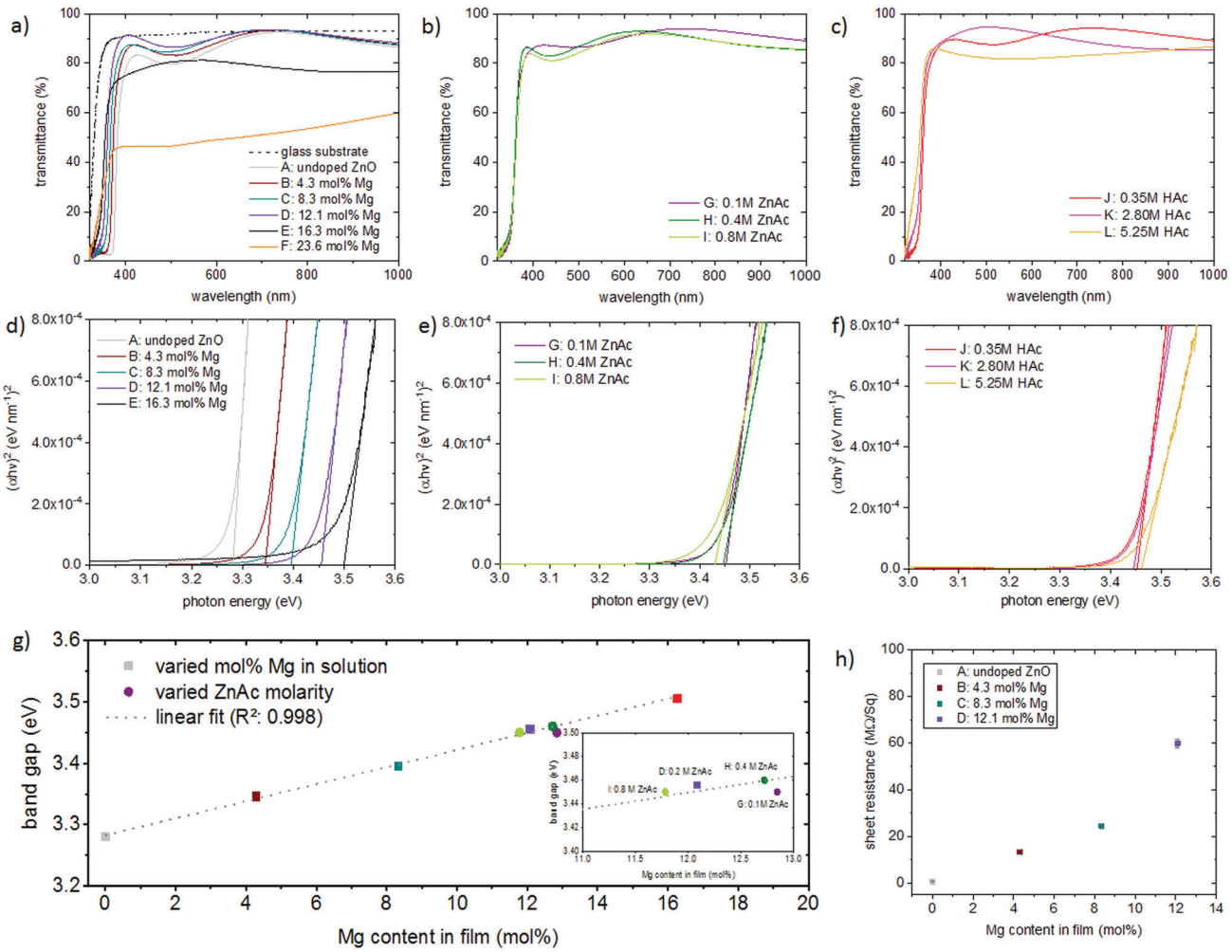

Fig. 13 FTIR transmittance spectra and Tauc plots for films deposited from solutions with (a) and (d) a variation in Mg concentration, (b) and (e) a variation in zinc acetate molarity, and (c) and (f) a variation in acetic acid concentration; (g) band gap as a function of the Mg content; and (h) sheet resistance as a function of the Mg content.

direct band gap semiconductors,[61] where α is the absorption coefficient, $h\nu$ the photon energy, A a constant and E_g is the band gap (in eV):

$$(\alpha \times h\nu)^2 = A \times (h\nu - E_g) \quad (1)$$

Fig. 13(d) shows a gradual band edge shift to higher values with increasing amounts of incorporated Mg. It was seen that there is a linear dependence of the band gap with Mg incorporation between 0 and 16.3 mol%. For the $Zn_{1-x}Mg_xO$ films realized by variations in the zinc acetate molarity, the optical band gap remained ~3.45 eV, as seen in Fig. 13(e). Alterations in the acetic acid concentration did not affect the band gap as well, as displayed in Fig. 13(f). Fig. 13(g) shows the dependence of the band gap on the amount of incorporated Mg for the different films.

The sheet resistance was measured for $Zn_{1-x}Mg_xO$ films (~250 nm thick) deposited on glass (as shown in Fig. 2(a)–(d)) with different Mg content (Fig. 13(h)). While for undoped ZnO the sheet resistance is 0.52 MΩ Sq^{-1}, it increases with an increasing amount of incorporated Mg to ~60 MΩ Sq^{-1} for films with 12 mol% incorporated Mg. This behaviour is commonly observed for $Zn_{1-x}Mg_xO$ films.[62]

3.3. $Zn_{1-x}Mg_xO$ deposited on TCO substrates

To show the applicability of the deposition process, $Zn_{1-x}Mg_xO$ films were sprayed onto three conducting oxide substrates, namely commercial FTO, ITO and sprayed IZO. This is an important step towards device applications in which $Zn_{1-x}Mg_xO$ is applied on a transparent electrode, such as solar cells with a superstrate architecture. It is important to note that the proposed deposition process might not be applicable to devices in which the substrate properties are impaired by the temperature and/or incoming vapor of precursor solution species.

It is well known that the nature of the substrate influences the surface texture of spray deposited films.[63–65] This behaviour can be attributed to the difference in surface energy and thermal properties for each substrate. As stated before, the heat conductivity of the substrate and the deposited material influences the morphology of the sprayed $Zn_{1-x}Mg_xO$. Therefore, a lower amount of nanorods in the deposited film is expected due to the higher heat

 This journal is © The Royal Society of Chemistry 2019

Open Access Article. Published on 13 March 2019. Downloaded on 1/14/2026 9:50:56 AM.
This article is licensed under a Creative Commons Attribution 3.0 Unported Licence.

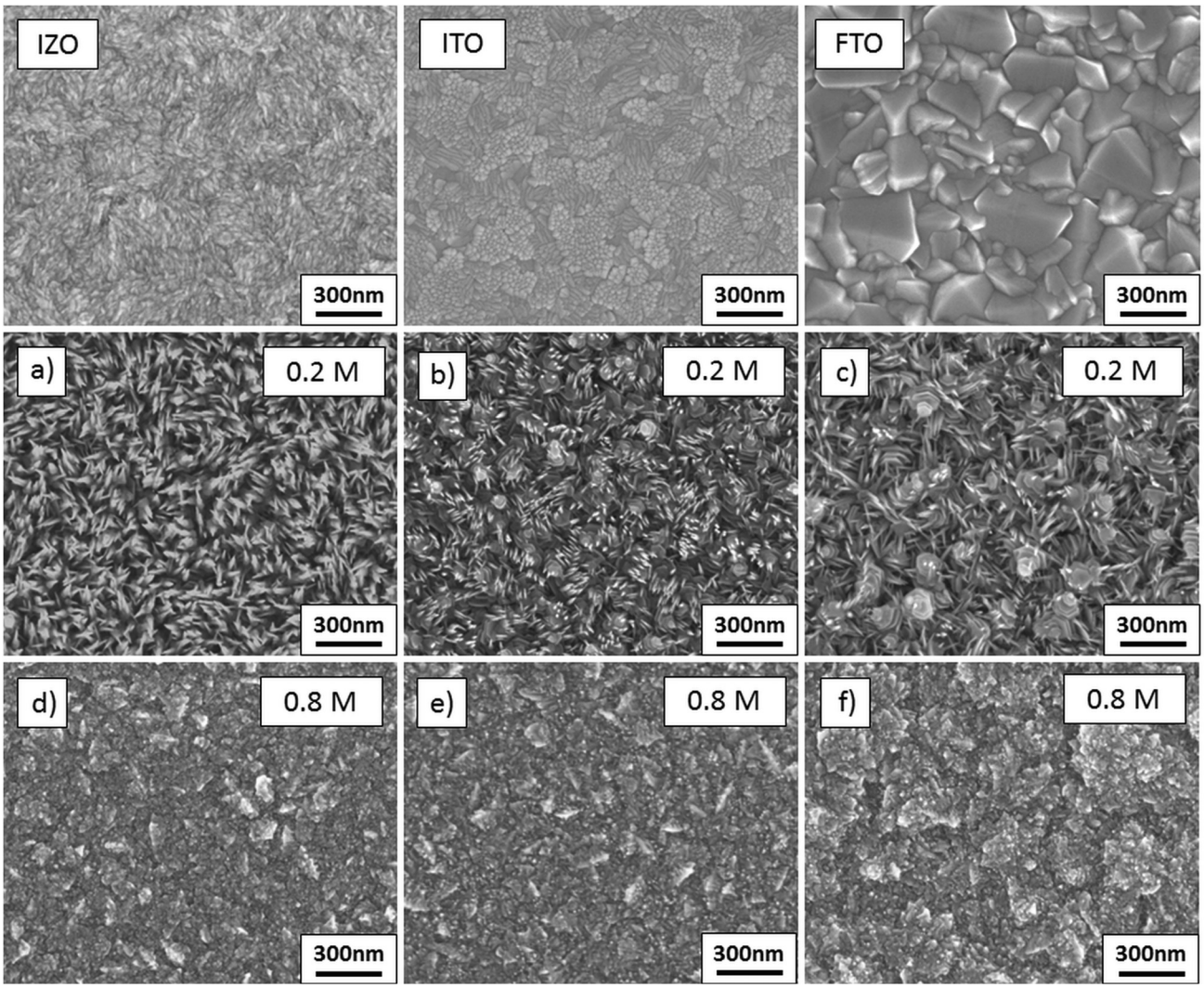

Fig. 14 SEM images of films deposited from solutions D (a–c) and I (d–f) on IZO (a and d); ITO (b and e); and FTO (c and f).

conductivity of metal oxide coated glass substrates, compared to pure borosilicate glass used in the previous experiments. To show that nanorods and dense $Zn_{0.88}Mg_{0.12}O$ films can be deposited, solution D (for nanorod formation) and solution I (for dense films) were used for the deposition on the various TCO substrates.

The film morphologies are displayed in Fig. 14(a)–(f). On all three TCO substrates it was observed that low concentration solutions (solution D) still lead to the formation of nanorods, while if the $ZnAc_2$ molarity is increased to 0.8 M compact films can be deposited. Nevertheless, deposition on ITO and FTO results in a lower amount of nanorods. This suggests that the main influence on the morphology of the deposited material stems from the solution composition and the underlying substrate has a minor effect on the film structure. The $Zn_{0.88}Mg_{0.12}O$ film morphology on FTO substrates (Fig. 14(f)) appears to be rougher than on the other two substrates, which arises from the rougher morphology of the underlying FTO substrate.

The film structure was further analysed by XRD diffractograms of $Zn_{0.88}Mg_{0.12}O$ deposited on ITO and FTO as shown in Fig. 15(a) and (b). Because of the high film thickness of the IZO electrode (1.8 μm) and the same crystal structure of IZO and $Zn_{0.88}Mg_{0.12}O$, it is not possible to assign specific peaks to $Zn_{0.88}Mg_{0.12}O$, therefore these diffractograms are not shown here.

On ITO substrates, the higher $ZnAc_2$ molarity results in the appearance of the $\{10\bar{1}0\}$ $Zn_{0.88}Mg_{0.12}O$ reflection additionally to $\{0001\}$, $\{10\bar{1}1\}$ and minor reflections of $\{11\bar{2}2\}$, while the $\{10\bar{1}2\}$ reflection disappears. On FTO substrates the $\{10\bar{1}0\}$ peak becomes more prominent with higher $ZnAc_2$ molarity, while $\{10\bar{1}2\}$ and $\{10\bar{1}3\}$ reflections could not be observed anymore. In comparison to that, on glass (Fig. 10(a)) the intensity of the $\{10\bar{1}0\}$, $\{10\bar{1}1\}$ and $\{11\bar{2}0\}$ reflections increased with increasing zinc acetate molarity. This shows that the substrate has only a minor additional influence on the film orientation.

In summary, results from the deposition on glass substrates can be transferred to other substrates such as glass coated with TCOs, without altering the material properties. This indicates that the proposed deposition process of $Zn_{1-x}Mg_xO$ can further be applied in various device applications. An example is given by the application of a compact $Zn_{0.88}Mg_{0.12}O$ film as a buffer layer in all-solution processed Cu_2O-type all-oxide solar cells.[47]

Open Access Article. Published on 13 March 2019. Downloaded on 1/14/2026 9:50:56 AM.
This article is licensed under a Creative Commons Attribution 3.0 Unported Licence.

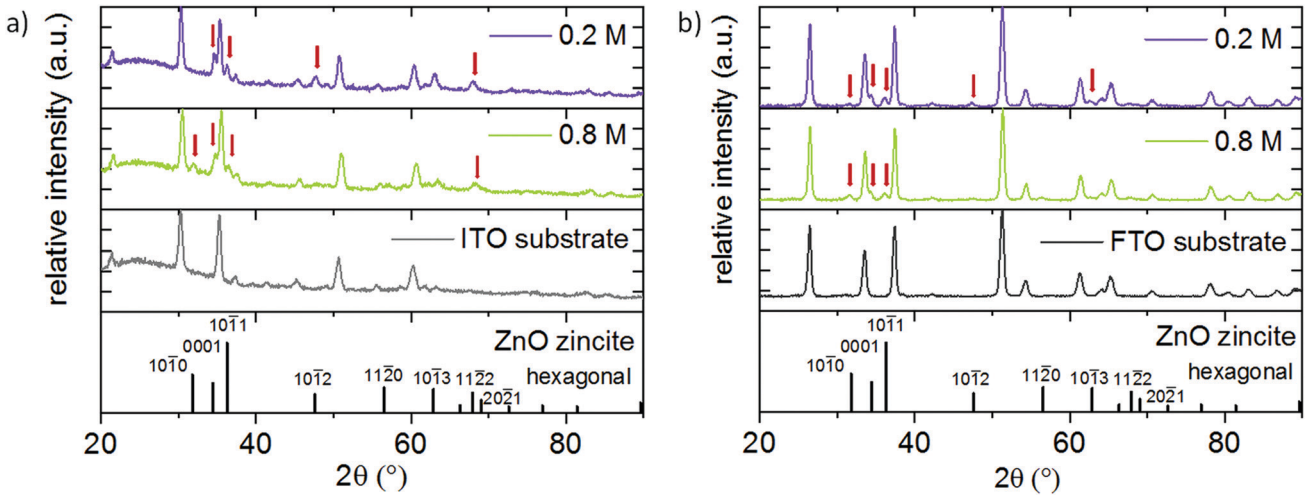

Fig. 15 XRD diffractograms of films deposited from solution D and I (a) on ITO, and (b) on FTO.

4. Conclusion

This article investigates the influence of the precursor solution composition on the structure of $Zn_{1-x}Mg_xO$ obtained by ultrasonic spray pyrolysis from water-based solutions. Depending on the precursor concentrations, either dense films or nanorods can be obtained. XRD in combination with ICP OES showed that Mg is substitutionally incorporated into the ZnO lattice. It was found that solely the precursor solution defines the amount of incorporated Mg, independent from the $Zn_{1-x}Mg_xO$ morphology, which offers a valuable tool to deposit nanostructures with defined amounts of Mg and band gaps between 3.28 and 3.50 eV. The applicability of the spray deposited $Zn_{1-x}Mg_xO$ nanostructures was demonstrated by deposition on conducting metal oxide substrates.

Conflicts of interest

There are no conflicts of interest to declare.

Acknowledgements

The authors thank Dr Oskar Armbruster for valuable discussions on the $Zn_{1-x}Mg_xO$ nanorod formation, Wolfgang Obermaier for the ICP OES measurements and Stephan Puchegger for EDX analysis at the University of Vienna.

References

1 A. Pérez-Tomás, E. Chikoidze, M. R. Jennings, S. A. O. Russell, F. H. Teherani, P. Bove, E. V. Sandana and D. J. Rogers, in *Oxide-based Materials and Devices IX*, International Society for Optics and Photonics, 2018, vol. 10533, p. 105331Q.
2 S. Calnan, Applications of Oxide Coatings in Photovoltaic Devices, *Coatings*, 2014, **4**, 162–202.
3 E. Fortunato, D. Ginley, H. Hosono and D. C. Paine, Transparent Conducting Oxides for Photovoltaics, *MRS Bull.*, 2007, **32**, 242–247.
4 Y.-J. Lee, D. S. Ruby, D. W. Peters, B. B. McKenzie and J. W. P. Hsu, ZnO Nanostructures as Efficient Antireflection Layers in Solar Cells, *Nano Lett.*, 2008, **8**, 1501–1505.
5 L. Spanhel, Colloidal ZnO nanostructures and functional coatings: A survey, *J. Sol-Gel Sci. Technol.*, 2006, **39**, 7–24.
6 W. Fuhs, *Zinc Oxide—A Material for Micro- and Optoelectronic Applications*, Springer, Dordrecht, 2005, pp. 197–209.
7 S. J. Pearton and F. Ren, Wide Band gap Semiconductor One-Dimensional Nanostructures for Applications in Nanoelectronics and Nanosensors, *Nanomater. Nanotechnol.*, 2013, **3**, 1.
8 A. B. Djurišić, A. M. C. Ng and X. Y. Chen, ZnO nanostructures for optoelectronics: Material properties and device applications, *Prog. Quantum Electron.*, 2010, **34**, 191–259.
9 B. S. Kang, H.-T. Wang, L.-C. Tien, F. Ren, B. P. Gila, D. P. Norton, C. R. Abernathy, J. Lin and S. J. Pearton, Wide Band gap Semiconductor Nanorod and Thin Film Gas Sensors, *Sensors (Basel)*, 2006, 6, 643–666.
10 L. Zhu and W. Zeng, Room-temperature gas sensing of ZnO-based gas sensor: A review, *Sens. Actuators, A*, 2017, **267**, 242–261.
11 A. Kołodziejczak-Radzimska, T. Jesionowski, A. Kołodziejczak-Radzimska and T. Jesionowski, Zinc Oxide—From Synthesis to Application: A Review, *Materials*, 2014, **7**, 2833–2881.
12 L. Schmidt-Mende and J. L. MacManus-Driscoll, ZnO–nanostructures, defects, and devices, *Mater. Today*, 2007, **10**, 40–48.
13 D. P. Norton, Y. W. Heo, M. P. Ivill, K. Ip, S. J. Pearton, M. F. Chisholm and T. Steiner, ZnO: growth, doping & processing, *Mater. Today*, 2004, **7**, 34–40.
14 A. Janotti and C. G. V. de Walle, Fundamentals of zinc oxide as a semiconductor, *Rep. Prog. Phys.*, 2009, **72**, 126501.
15 M. Rouchdi, E. Salmani, B. Fares, N. Hassanain and A. Mzerd, Synthesis and characteristics of Mg doped ZnO thin films: Experimental and ab-initio study, *Results Phys.*, 2017, **7**, 620–627.
16 D. Hariskos, B. Fuchs, R. Menner, N. Naghavi, C. Hubert, D. Lincot and M. Powalla, The Zn(S,O,OH)/ZnMgO buffer in

Open Access Article. Published on 13 March 2019. Downloaded on 1/14/2026 9:50:56 AM.
This article is licensed under a Creative Commons Attribution 3.0 Unported Licence.

thin-film Cu(In,Ga)(Se,S)$_2$-based solar cells part II: Magnetron sputtering of the ZnMgO buffer layer for in-line co-evaporated Cu(In,Ga)Se$_2$ solar cells, *Prog. Photovoltaics*, 2009, **17**, 479–488.

17 T. Minami, Y. Nishi, T. Miyata and S. Abe, Photovoltaic Properties in Al-doped ZnO/non-doped $Zn_{1-x}MgXO/Cu_2O$ Heterojunction Solar Cells, *ECS Trans.*, 2013, **50**, 59–68.

18 A. Ohtomo, M. Kawasaki, T. Koida, K. Masubuchi, H. Koinuma, Y. Sakurai, Y. Yoshida, T. Yasuda and Y. Segawa, $Mg_xZn_{1-x}O$ as a II–VI widegap semiconductor alloy, *Appl. Phys. Lett.*, 1998, **72**, 2466–2468.

19 T. Minemoto, T. Negami, S. Nishiwaki, H. Takakura and Y. Hamakawa, Preparation of $Zn_{1-x}Mg_xO$ films by radio frequency magnetron sputtering, *Thin Solid Films*, 2000, **372**, 173–176.

20 K. Ogata, K. Koike, T. Tanite, T. Komuro, F. Yan, S. Sasa, M. Inoue and M. Yano, ZnO and ZnMgO growth on a-plane sapphire by molecular beam epitaxy, *J. Cryst. Grow.*, 2003, **251**, 623–627.

21 T. Törndahl, C. Platzer-Björkman, J. Kessler and M. Edoff, Atomic layer deposition of $Zn_{1-x}Mg_xO$ buffer layers for Cu(In,Ga)Se$_2$ solar cells, *Prog. Photovoltaics*, 2007, **15**, 225–235.

22 N. Winkler, S. Edinger, W. Kautek and T. Dimopoulos, Mg-doped ZnO films prepared by chemical bath deposition, *J. Mater. Sci.*, 2018, **53**, 5159–5171.

23 M. Wang, J. Yi, S. Yang, Z. Cao, X. Huang, Y. Li, H. Li and J. Zhong, Electrodeposition of Mg doped ZnO thin film for the window layer of CIGS solar cell, *Appl. Surf. Sci.*, 2016, **382**, 217–224.

24 M. Wang, E. J. Kim, S. Kim, J. S. Chung, I.-K. Yoo, E. W. Shin, S. H. Hahn and C. Park, Optical and structural properties of sol–gel prepared MgZnO alloy thin films, *Thin Solid Films*, 2008, **516**, 1124–1129.

25 E. R. Segnit and A. E. Holland, The System MgO–ZnO–SiO$_2$, *J. Am. Ceram. Soc.*, 1965, **48**, 409–413.

26 F. Paraguay D., W. Estrada L., D. R. Acosta N., E. Andrade and M. Miki-Yoshida, Growth, structure and optical characterization of high quality ZnO thin films obtained by spray pyrolysis, *Thin Solid Films*, 1999, **350**, 192–202.

27 E. Arca, K. Fleischer and I. V. Shvets, Influence of the Precursors and Chemical Composition of the Solution on the Properties of ZnO Thin Films Grown by Spray Pyrolysis, *J. Phys. Chem. C*, 2009, **113**, 21074–21081.

28 G. Adamopoulos, A. Bashir, W. P. Gillin, S. Georgakopoulos, M. Shkunov, M. A. Baklar, N. Stingelin, D. D. C. Bradley and T. D. Anthopoulos, Structural and Electrical Characterization of ZnO Films Grown by Spray Pyrolysis and Their Application in Thin-Film Transistors, *Adv. Funct. Mater.*, 2011, **21**, 525–531.

29 W.-N. Wang, A. Purwanto, I. W. Lenggoro, K. Okuyama, H. Chang and H. D. Jang, Investigation on the Correlations between Droplet and Particle Size Distribution in Ultrasonic Spray Pyrolysis, *Ind. Eng. Chem. Res.*, 2008, **47**, 1650–1659.

30 M. Lopez-Ponce, A. Hierro, V. Marín-Borrás, G. Tabares, A. Kurtz, S. Albert, S. Agouram, V. Muñoz-Sanjosé, E. Muñoz and J. M. Ulloa, Optical properties of ZnMgO films grown by spray pyrolysis and their application to UV photodetection, *Semicond. Sci. Technol.*, 2015, **30**, 105026.

31 K. Hoggas, C. Nouveau, A. Djelloul and M. Bououdina, Structural, microstructural, and optical properties of $Zn_{1-x}Mg_xO$ thin films grown onto glass substrate by ultrasonic spray pyrolysis, *Appl. Phys. A: Mater. Sci. Process.*, 2015, **120**, 745–755.

32 W. S. Choi and J.-G. Yoon, Optical characterization of band gap graded ZnMgO films, *Solid State Commun.*, 2012, **152**, 345–348.

33 K. Vijayalakshmi and A. Renitta, Enhanced H2 sensing performance presented by Mg doped ZnO films fabricated with a novel ITO seed layer, *J. Mater. Sci.: Mater. Electron.*, 2015, **26**, 3458–3465.

34 M. Sahal, B. Marí, M. Mollar and F. J. Manjón, $Zn_{1-x}Mg_xO$ thin films deposited by spray pyrolysis, *Phys. Status Solidi C*, 2010, **7**, 2306–2310.

35 T. Terasako, S. Shirakata and T. Kariya, Photoluminescence from highly oriented $Mg_xZn_{1-x}O$ films grown by chemical spray pyrolysis, *Thin Solid Films*, 2002, **420**, 13–18.

36 E. Diler, S. Rioual, B. Lescop, D. Thierry and B. Rouvellou, Stability of ZnMgO oxide in a weak alkaline solution, *Thin Solid Films*, 2012, **520**, 2819–2823.

37 X. Zhang, X. M. Li, T. L. Chen, C. Y. Zhang and W. D. Yu, p-type conduction in wide-gap $Zn_{1-x}Mg_xO$ films grown by ultrasonic spray pyrolysis, *Appl. Phys. Lett.*, 2005, **87**, 092101.

38 H. Zhang, T. Zhao, G. Hu, L. Miao and Y. Yang, Role of Mg doping on morphology and photoluminescence features of $Mg_xZn_{1-x}O$ films prepared by ultrasonic spray pyrolysis, *J. Mater. Sci.: Mater. Electron.*, 2012, **23**, 1933–1937.

39 K. Yoshino, S. Oyama and M. Yoneta, Structural, optical and electrical characterization of undoped ZnMgO film grown by spray pyrolysis method, *J. Mater. Sci.: Mater. Electron.*, 2008, **19**, 203–209.

40 A. J. Kulandaisamy, J. R. Reddy, P. Srinivasan, K. J. Babu, G. K. Mani, P. Shankar and J. B. B. Rayappan, Room temperature ammonia sensing properties of ZnO thin films grown by spray pyrolysis: Effect of Mg doping, *J. Alloys Compd.*, 2016, **688**, 422–429.

41 S. Kurtaran, S. Aldag, G. Ofofoglu, I. Akyuz and F. Atay, Transparent conductive ZnO thin films grown by chemical spray pyrolysis: the effect of Mg, *J. Mater. Sci.: Mater. Electron.*, 2016, **27**, 8478–8485.

42 P. Ravirajan, A. M. Peiró, M. K. Nazeeruddin, M. Graetzel, D. D. C. Bradley, J. R. Durrant and J. Nelson, Hybrid Polymer/Zinc Oxide Photovoltaic Devices with Vertically Oriented ZnO Nanorods and an Amphiphilic Molecular Interface Layer, *J. Phys. Chem. B*, 2006, **110**, 7635–7639.

43 J. X. Wang, X. W. Sun, Y. Yang, H. Huang, Y. C. Lee, O. K. Tan and L. Vayssieres, Hydrothermally grown oriented ZnO nanorod arrays for gas sensing applications, *Nanotechnology*, 2006, **17**, 4995.

44 M. Ding, Z. Guo, L. Zhou, X. Fang, L. Zhang, L. Zeng, L. Xie, H. Zhao, M. Ding, Z. Guo, L. Zhou, X. Fang, L. Zhang, L. Zeng, L. Xie and H. Zhao, One-Dimensional Zinc Oxide Nanomaterials for Application in High-Performance Advanced Optoelectronic Devices, *Crystals*, 2018, **8**, 223.

45 İ. Polat, S. Yılmaz, E. Bacaksız, Y. Atasoy and M. Tomakin, Synthesis and fabrication of Mg-doped ZnO-based dye-synthesized solar cells, *J. Mater. Sci.: Mater. Electron.*, 2014, **25**, 3173–3178.

Open Access Article. Published on 13 March 2019. Downloaded on 1/14/2026 9:50:56 AM.
This article is licensed under a Creative Commons Attribution 3.0 Unported Licence.

46 T.-H. Fang and S.-H. Kang, Preparation and characterization of Mg-doped ZnO nanorods, *J. Alloys Compd.*, 2010, **492**, 536–542.
47 N. Winkler, S. Edinger, J. Kaur, R. A. Wibowo, W. Kautek and T. Dimopoulos, Solution-processed all-oxide solar cell based on electrodeposited Cu_2O and ZnMgO by spray pyrolysis, *J. Mater. Sci.*, 2018, 1–13.
48 R. D. Shannon, Revised effective ionic radii and systematic studies of interatomic distances in halides and chalcogenides, *Acta Crystallogr., Sect. A: Cryst. Phys., Diffr., Theor. Gen. Crystallogr.*, 1976, **32**, 751–767.
49 Y. Cai, X. Li, P. Sun, B. Wang, F. Liu, P. Cheng, S. Du and G. Lu, Ordered ZnO nanorod array film driven by ultrasonic spray pyrolysis and its optical properties, *Mater. Lett.*, 2013, **112**, 36–38.
50 U. Alver, T. Kılınç, E. Bacaksız, T. Küçükömeroğlu, S. Nezir, İ. H. Mutlu and F. Aslan, Synthesis and characterization of spray pyrolysis Zinc Oxide microrods, *Thin Solid Films*, 2007, **515**, 3448–3451.
51 E. Kärber, T. Raadik, T. Dedova, J. Krustok, A. Mere, V. Mikli and M. Krunks, Photoluminescence of spray pyrolysis deposited ZnO nanorods, *Nanoscale Res. Lett.*, 2011, **6**, 359.
52 T. Arii and A. Kishi, The effect of humidity on thermal process of zinc acetate, *Thermochim. Acta*, 2003, **400**, 175–185.
53 F. Hewitt, D. E. Rhebat, A. Witkowski and T. R. Hull, An experimental and numerical model for the release of acetone from decomposing EVA containing aluminium, magnesium or calcium hydroxide fire retardants, *Polym. Degrad. Stab.*, 2016, **127**, 65–78.
54 O. F. Z. Khan and P. O'Brien, On the use of zinc acetate as a novel precursor for the deposition of ZnO by low-pressure metal-organic chemical vapour deposition, *Thin Solid Films*, 1989, **173**, 95–97.
55 L. Hiltunen, M. Leskelä, M. Mäkelä and L. Niinistö, Crystal Structure of mu4-Oxo-hexakis(mu-acetato)tetrazinc and Thermal Studies of its Precursor, Zinc Acetate Dihydrate, *Acta Chem. Scand.*, 1987, **41a**, 548–555.
56 C. W. Bock, A. K. Katz, G. D. Markham and J. P. Glusker, Manganese as a Replacement for Magnesium and Zinc: Functional Comparison of the Divalent Ions, *J. Am. Chem. Soc.*, 1999, **121**, 7360–7372.
57 T. Dudev and C. Lim, Tetrahedral vs Octahedral Zinc Complexes with Ligands of Biological Interest: A DFT/CDM Study, *J. Am. Chem. Soc.*, 2000, **122**, 11146–11153.
58 S. Shanmugan and D. Mutharasu, Thermal analysis of Mg doped ZnO nano particles as filler in epoxy for thermal interface material in led packaging, *J. Optoelectron. Biomed. Mater.*, 2016, **8**, 1–7.
59 T. Tsubota, M. Ohtaki, K. Eguchi and H. Arai, Transport properties and thermoelectric performance of $(Zn_{1-y}Mg_y)_{1-x}Al_xO$, *J. Mater. Chem.*, 1998, **8**, 409–412.
60 S. Edinger, J. Bekacz, M. Richter, R. Hamid, R. A. Wibowo, A. Peić and T. Dimopoulos, Influence of the acetic acid concentration on the growth of zinc oxide thin films prepared by spray pyrolysis of aqueous solutions, *Thin Solid Films*, 2015, **594**, 238–244.
61 J. Tauc, Optical properties and electronic structure of amorphous Ge and Si, *Mater. Res. Bull.*, 1968, **3**, 37–46.
62 A. Kaushal and D. Kaur, Effect of Mg content on structural, electrical and optical properties of $Zn_{1-x}Mg_xO$ nanocomposite thin films, *Sol. Energy Mater. Sol. Cells*, 2009, **93**, 193–198.
63 E. Bingöl, F. Bozali, E. F. Keskenler, V. Nevruzoğlu and M. Tomakin, Influence of Substrate Type on Morphology and Photoluminescence Properties of ZnO Thin Films Prepared by Ultrasonic Spray Pyrolysis Method, *Turk. J. Mater.*, 2016, **1**, 19–24.
64 S. M. Thahab, A. H. Omran Alkhayat and S. M. Saleh, Influence of substrate type on the structural, optical and electrical properties of $CdxZn_{1-x}S$ MSM thin films prepared by Spray Pyrolysis method, *Mater. Sci. Semicond. Process.*, 2014, **26**, 49–54.
65 I. Oja Acik, A. Junolainen, V. Mikli, M. Danilson and M. Krunks, Growth of ultra-thin TiO_2 films by spray pyrolysis on different substrates, *Appl. Surf. Sci.*, 2009, **256**, 1391–1394.

 This journal is © The Royal Society of Chemistry 2019